A Morphology-Based Approach for Interslice Interpolation of Anatomical Slices From Volumetric Images

Alexandra Branzan Albu*, *Member, IEEE*, Trevor Beugeling, and Denis Laurendeau, *Member, IEEE*

***Abstract*—This paper proposes a new morphology-based approach for the interslice interpolation of current transformer (CT) and MRI datasets composed of parallel slices. Our approach is object based and accepts as input data binary slices belonging to the same anatomical structure. Such slices may contain one or more regions, since topological changes between two adjacent slices may occur. Our approach handles explicitly interslice topology changes by decomposing a many-to-many correspondence into three fundamental cases: one-to-one, one-to-many, and zero-to-one correspondences. The proposed interpolation process is iterative. One iteration of this process computes a transition sequence between a pair of corresponding input slices, and selects the element located at equal distance from the input slices. This algorithmic design yields a gradual, smooth change of shape between the input slices. Therefore, the main contribution of our approach is its ability to interpolate between two anatomic shapes by creating a smooth, gradual change of shape, and without generating over-smoothed interpolated shapes.**

***Index Terms*—Mathematical morphology, shape-based interpolation, volumetric imaging.**

I. Introduction

WIDELY used medical imaging systems based on magnetic resonance (MR), computer-assisted tomography (CT), or 3-D ultrasound technologies generate serial sequences of 2-D parallel image slices as an end result of the scanning process. In most cases, the volumetric nature of this data does not play an important role in diagnosis. Indeed, clinical radiologists still base their diagnosis upon visual examination, and approximate measurements performed manually on selected 2-D images of the sequence. Emerging interactive 3-D data measurement and visualization techniques are expected to support healthcare professionals in improving the accuracy of image-based diagnosis and therapy planning.

In order to efficiently visualize, analyze, and manipulate data from serial CT or MR sequences, one has to deal with the difference between the inter- and intraslice resolutions. This difference is due to technical and physiological limitations in the image acquisition process such as respiratory motion, maximal radiation dose, and device-specific noise. The visualization of 3-D anisotropic data featuring an intraslice resolution much higher than the interslice resolution is unrealistic and not suitable for diagnosis or therapy planning purposes. This is the reason why interpolation techniques are useful for estimating "missing" slices, and therefore for increasing the interslice resolution.

Interslice interpolation is an ill-posed problem, since there is no unique solution to it. Furthermore, there is no objective criterion that can be used for measuring the "correctness" of an interpolated sequence. Whitaker [1] advocates the necessity of applying external, application-specific constraints for deciding how "good" an interpolation sequence is. Along the same line, Barequet and Vaxman [2] state the need of a heuristic in order to constrain the interpolation problem to a unique solution.

Techniques developed for various medical and nonmedical application domains have introduced a set of quasi-synonyms for interpolation such as morphing [3], [4], metamorphosis [5], [6], blending [1], and shape transformation [7]. We will further refer to this whole set of terms as shape morphing (the most widely used) in order to point out some differences between medical shape interpolation and morphing. Shape morphing deals with transforming shape A into shape B by building a sequence of intermediate shapes so that adjacent pairs in the sequence have a high level of geometric similarity. The applications area covered by shape morphing is much larger than the one corresponding to medical interslice interpolation. Therefore, the pairs of input shapes required for generating the morphing sequence are usually selected so that they exhibit large semantic and morphological differences (see visual examples in [3], [6], [7], etc.). Such an experimental design scheme is suitable for computer animation applications, as well as for simulation-oriented medical applications such as modeling postoperative growth in craniofacial surgery planning [4]. However, this experimental design is less adequate for the purpose of estimating "missing" slices in volumetric medical images, mainly because of two specific aspects of interslice shape variation in anatomical slices. First, two adjacent slices in a medical dataset exhibit some degree of similarity. Second, 2-D slices of anatomical structures such as organs or bone do not have smooth boundaries at typically used image scales.

A common criterion employed for evaluating the quality of a morphing sequence is related to how natural looking the transition from the first image to the second is [1]. This criterion can

Manuscript received December 12, 2006; revised January 5, 2008. This work was supported by the Natural Science and Engineering Research Council of Canada. *Asterisk indicates corresponding author.*

*A. Branzan Albu is with the Department of Electrical and Computer Engineering, University of Victoria, Victoria, BC V8 W 3P6, Canada (e-mail: aalbu@ece.uvic.ca).

T. Beugeling is with the Department of Electrical and Computer Engineering, University of Victoria, Victoria BC V8 W 3P6, Canada (e-mail: trjb@uvic.ca).

D. Laurendeau is with the Department of Electrical and Computer Engineering, Laval University, Quebec-City, QC G1 V 0A6, Canada (e-mail: denis.laurendeau@gel.ulaval.ca).

Color versions of one or more of the figures in this paper are available online at http://ieeexplore.ieee.org.

Digital Object Identifier 10.1109/TBME.2008.921158

0018-9294/$25.00 © 2008 IEEE

either take a subjective form (i.e., whether a human observer notices or not the difference between input shapes and morphed ones [1]), or it can be formulated as an objective measure of change smoothness. Some morphing techniques are designed so that they minimize a function of energy that is directly related to shape smoothness. However, change smoothness and the smoothness of morphed shapes are two different concepts. This difference plays a significant role in medical interslice interpolation, where the interpolated shapes need to preserve local "unsmooth" morphologic details present in one or both of the input shapes (concavities, invaginations, protrusions, etc.).

Medical interslice interpolation techniques can be classified into several categories with respect to the type of their input data, namely gray level, region based, and contour based; contours may be specified either as a set of sparse points or as closed planar curves. Gray-level or scene-based interpolation approaches compute directly the intensity for every pixel in the interpolated slice; such techniques include the nearest neighbor method described by Pratt [8], linear gray-level interpolation as proposed by Goldwasser *et al*. [9], higher order polynomial interpolation, and cubic spline interpolation [10]. As shown by Raya and Udupa [11], for medical imaging applications that are strongly object-oriented, grey-level interpolation techniques are not recommendable, since they result in a large amount of input data for further segmentation and in errors occurring in segmentation due to prior interpolation. Nevertheless, gray-level interpolation is suitable for applications that require the simultaneous interpolation of several anatomic structures present in the input slices, such as in abdominal CT scans. In addition, as shown in Penney *et al*. [12], gray-level interpolation may produce large artifacts when the planar location of anatomical features shifts significantly between slices; their method is able to eliminate these artifacts by using a voxel-based nonrigid registration algorithm for registering adjacent slices.

Grevera and Udupa [13] have shown that shape-based interpolation techniques are more efficient than gray-level interpolation methods. Shape-based techniques are object-oriented and aim at interpolating the binary object cross section, rather than gray-scale values. Werahera *et al*. proposed in [14] a linear shape-based interpolation technique using interslice centroid and neighborhood matching. The technique introduced by Raya and Udupa [11] is considered as the most representative of the shape-based interpolation class. This technique converts binary images containing only shape information into gray-level images via a distance transform which assigns to every point in the binary image a gray-level equal to its shortest distance from the cross-sectional boundary. This conversion enables the application of a standard gray-level interpolation technique, and it is followed by a reverse conversion to binary images. Recently, Saha *et al*. [15] proposed a fuzzy version of the approach in [11]; this version uses a fuzzy distance transform theory that is applicable to fuzzy object representations. The distance transform is also used by Lee and Lin [16]; they perform a distance interpolation guided by line segments. Treece *et al*. [17] propose a shape-based interpolation from sparse cross-sections using region correspondence for branching cases; their approach extends their earlier work on maximal disk-guided interpolation [18].

A level set reformulation of the method in [11] is presented by Morigi and Sgallari [19]. Their approach formulates the interpolation process with input images **u** and **v** as the evolution of each level set of **u** toward becoming more similar to the corresponding level set of **v** and vice versa. This approach works well if the 2-D boundaries of the corresponding structures in adjacent slices are well defined, which may not be the case in volumetric images; as shown by Souza *et al*. [20], the partial volume effect present in CT and MRI images may cause blurring artifacts at the boundary of anatomical structures. Whitaker [1] proposes a level set approach for gray-level image morphing, which relies on the gradual minimization of a difference metric that compares the level sets between two images. The contour morphing method proposed by Nilsson *et al*. [5] uses 2-D level sets for propagating closed contours at speeds that depend on the distance between the input contours. Their approach is focused on generating smooth surfaces that fit to an arbitrary number of parallel contours. Zhao *et al*. [21] use a variational level set method for reconstructing an implicit shape from unorganized input data consisting from sparse points, pieces of curves, and surface patches. They show that their reconstructed surfaces are smoother than piecewise linear reconstructions. Yang and Yuttler [6] propose an approach for morphing 3-D shapes based on T-spline level sets; this approach handles complex topology changes and produces smooth transitions between pairs of very different input 3D shapes (for instance, between an apple and a teapot).

In shape morphing, implicit surface modeling represents an efficient way of dealing with topological changes such as branching. Implicit surfaces can be built using level sets (see aforementioned) or other techniques.

For instance, Turk and O'Brien [7] propose a shape morphing approach based on variational interpolation, which solves simultaneously two tasks, namely shape description via implicit functions and shape interpolation. Their approach works with 2-D and 3-D contours specified as sets of sparse points representing boundary constraints and normal constraints. Akkouche and Galin [22] propose a method for surface reconstruction from a parallel stack of contours, where the reconstructed surface is defined implicitly. They compute the global implicit function as a combination of local implicit functions describing trapezoids built between every pair of adjacent contour slices.

One alternate approach to the implicit surface/volumetric modeling paradigm is explicit surface representation. Explicit representation allows for tracking topological events such as branching or interslice region correspondence problems (one-to-one, many-to-many). Surazhsky *et al*. [23] study the problem of interpolation between two slices of different topologies; they conclude that such a problem is ill-posed, since the change of topology can occur at the level of upper slice, the lower slice, or anywhere in between. Their solution is based on a heuristic that states that the topology should change in the middle of the interpolated sequence of slices. Recent work by Barequet and Vaxman [2] generates an explicit 3-D surface using a nonlinear interslice interpolation algorithm; this algorithm computes a flow graph for matching vertices belonging to the symmetric difference of the two input slices. Jeong and Radke [24] proposed a method for

an explicit interslice interpolation between input contours specified manually as sets of sparse points. Their method offers a solution to the one-to-one interslice correspondence problem by interpolating between sets of elliptic Fourier descriptors (EFDs) corresponding to the sequence of input contours.

As shown by Serra [25], mathematical morphology offers a rich set of tools for shape analysis, modeling, and interpolation. A shape-based interpolation methodology based on geodesics of the Hausdorff distance is described by Serra in [26]. An algorithm based on morphological skeleton matching for interpolating slices in a 3-D binary object is proposed by Chatzis and Pitas [27]. This algorithm first performs a skeleton interpolation, and then generates the shapes corresponding to the interpolated skeletons. While this approach works fine for the image sets shown in [27], its performance is not guaranteed on asymmetric, complex input shapes, mainly due to the well-known sensitivity of the morphological skeleton to noise. The interpolation technique proposed by Bors *et al*. [28] generates a new group of slices between each two consecutive image slices by performing iterative erosions of the boundary elements in the initial set corresponding to the background of the final set. Lee and Wang [29] describe an interpolation technique that uses morphological dilation for creating distance maps, followed by erosion to accomplish the interpolation. Their approach generalizes the one-to-one correspondence to the many-to-many case by using a simple surface overlap criterion. Our experiments showed that, when considering nonconvex or thin initial shapes, iterative erosions may divide the foreground in disjoint regions, thus creating a false topology change. This is the main reason why our proposed interpolation approach is based on dilation only.

This paper proposes a new morphology-based approach for interslice interpolation of CT and MRI datasets composed of parallel slices. The main contribution of our approach is its ability to interpolate between two anatomic shapes by creating a smooth, gradual change of shape, and without generating oversmoothed interpolated shapes. Our approach accepts as input data binary slices belonging to the same anatomical structure. Such slices may contain one or more regions, since topological changes between two adjacent slices may occur. Therefore, our approach handles one-to-one, one-to-many, and many-to-many region correspondence cases. Prior to interpolation, corresponding regions are aligned via a minimum displacement for a maximum overlap criterion; we prove that this new criterion is more suitable than the traditional centroid matching [29]. Interpolation between two corresponding regions located in adjacent slices is performed by using a novel iterative dilation-based algorithm.

The remainder of the paper is structured as follows. Section II describes the proposed approach. Section III presents the experimental validation of the proposed approach. Section III draws conclusions and describes future work.

II. Proposed Approach

The main steps of the proposed approach are outlined in Fig. 1. For clarity purposes, this flowchart describes only one iteration of the interpolation process. The interslice interpolation is performed iteratively by generating one slice at a time between each pair of adjacent input slices until the desired interslice resolution is reached (see Section II-A); slices interpolated at a given iteration step become input for the next iteration. A visual example of one iteration of interslice interpolation accompanies the flowchart. This particular example shows how a branching correspondence case is first transformed into two parallel one-to-one correspondence cases, which are further submitted to interpolation using conditional dilation. The main steps of the proposed approach are described in the following sections.

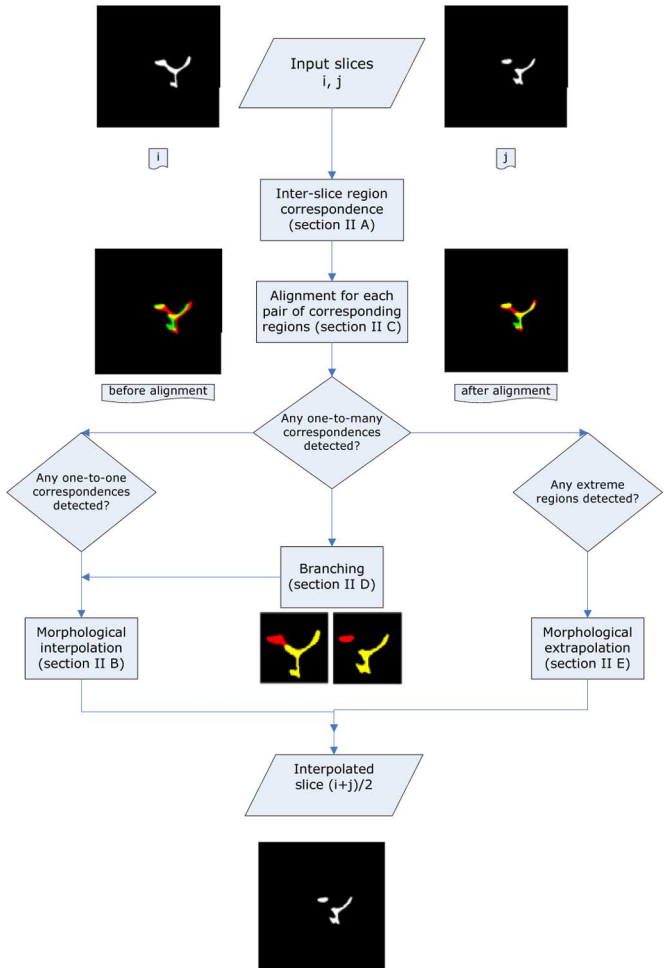

Fig. 1. One iteration in the proposed interslice interpolation approach.

A. Interslice Region Correspondence

The proposed approach is designed for handling input slices belonging to one anatomical structure. Since volumetric medical images typically contain more than one structure, parallel interpolation processes (one per each anatomical structure) can be performed. Thus, this paper assumes that the correspondence of planar regions and anatomical structures is already identified by the prior segmentation process (manual, semiautomatic, or automatic).

For two adjacent slices in a given anatomical structure, there are three basic cases of interslice region correspondence; they are discussed later and illustrated in Fig. 2. An arbitrary many-to-many interslice correspondence case is a combination of these three basic cases. Similar taxonomies for handling explicit

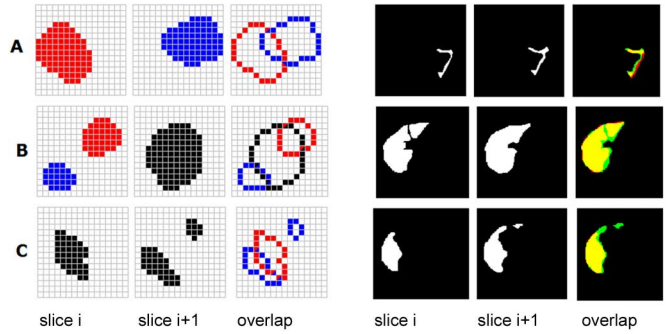

Fig. 2. Three basic cases of interslice region correspondence in serial sequences of parallel slices. Left, synthetic images; right, real slices from experimental dataset (overlap is in yellow). (a) One-to-one region correspondence. (b) One-to-many region correspondence (branching). (c) Zero-to-one region correspondence (extreme region) in the upper right corner of slice $i+1$.

interslice correspondence have been used by Barequet *et al.* [30] and Gabrielides *et al.* [31]. The main assumption underlying our taxonomy is partial overlap between corresponding regions. While this assumption is verified for a wide morphological variety of anatomical structures scanned with current CT and MRI technologies, there may be cases where a significant shift occurs between corresponding regions in two adjacent slices. This shift can be caused either by a large slice thickness or by the morphology of the structure (for instance, thin blood vessels with "slanted" orientation with respect to the slice plane). The proposed approach does not handle cases where corresponding regions do not partially overlap in adjacent slices.

The three possible cases of interslice correspondence handled by our approach are as follows:

1) *one-to-one correspondence:* In each of the adjacent slices i and $i+1$, the object is represented by one connected region [Fig. 2(a)]; these two regions are partially overlapping;
2) *one-to-many correspondence ("branching"):* The same object is represented by one region in slice $i+1$, and by two or more regions in slice i [Fig. 2(b)] or vice versa. As in case 1), there is a partial overlap between every region in slice i (the "branches") and the region in slice $i+1$ (the "trunk");
3) *zero-to-one correspondence ("extreme" regions):* Given slices i and $i+1$, an "extreme" region in slice $i+1$ is defined as a region having no overlap with any regions in slice i. Extreme regions typically occur when a new branch begins, ends, or at the extremities of structures. A zero-to-many correspondence signifies the appearance of several branches in the same slice, and it can be decomposed into several zero-to-one correspondences. Extreme regions are handled by the extrapolation process described in Section II-E.

B. Morphology-Based Interpolation

The proposed approach for interpolation works with aligned shapes. Alignment is discussed in Section II-C, since the rationale for the proposed alignment method is based on how the interpolation works.

1) Mathematical Background: Mathematical morphology considers 2-D binary images as sets of pixels on which set operations such as translation, union, and intersection can be performed. The *dilation* of set A using the structuring element K is defined as

$$A \oplus K = \cup\{A_k \,|k \in K\} \tag{1}$$

where $\oplus$ stands for the dilation operator, A_k is the translated set A, centered at an element k in K, and K is a structuring element. In this study, we chose a cross-shaped element derived from the four-connectivity neighborhood in the image lattice.

The *conditional dilation operator* is derived from the standard dilation as follows.

Definition: Let A and B be two discrete sets in the same image lattice, such that $B \subset A$. The *conditional dilation* of set B using the structuring element K and with respect to reference set A is defined as

$$B \oplus_A K = (B \oplus K) \cap A. \tag{2}$$

It is proven by Serra [25] that a finite number m of iterative conditional dilations with respect to A is required to generate A from B as

$$B \oplus_A^m K = \underbrace{(\ldots((B \oplus_A K) \oplus_A K) \ldots \oplus_A K)}_{m \text{ times}}. \tag{3}$$

2) Morphology-Based Interpolation for the One-to-One Correspondence Case: The proposed interpolation technique generates a smooth, gradual transition between two given binary regions denoted by A and B. The following set of conditions is verified by the initial regions:

1) A and B are connected with no interior holes;
2) A and B are partially overlapping.

Although holes are frequently encountered in soft tissue organs (e.g., liver vessels may be considered as holes in the liver), condition 1) is easy to satisfy either by using a morphological filling or by considering the outer boundary only. Condition 2) has been discussed in Section II-A.

The interpolation algorithm creates a *transition sequence* by using two parallel deformation processes based on iterative conditional dilation. The convergence of these processes is granted by (3).

The first process transforms the intersection $A \cap B$ into region A using l_A iterative conditional dilations, with A as reference region and K as structuring element. Similarly, the second process transforms the intersection $A \cap B$ into region B using l_B iterative conditional dilations, with B as reference region and K as structuring element. The mathematical description of these two processes is given by

$$\begin{aligned} \text{dilatcond}\,(A \cap B; A; i) &= (A \cap B) \oplus_A^i K, \qquad i = 1, \ldots, l_A \\ \text{dilatcond}\,(A \cap B; B; i) &= (A \cap B) \oplus_B^i K, \qquad i = 1, \ldots, l_B. \end{aligned} \tag{4}$$

The proposed interpolation scheme combines the previous two dilational processes and creates a transition sequence *seq*

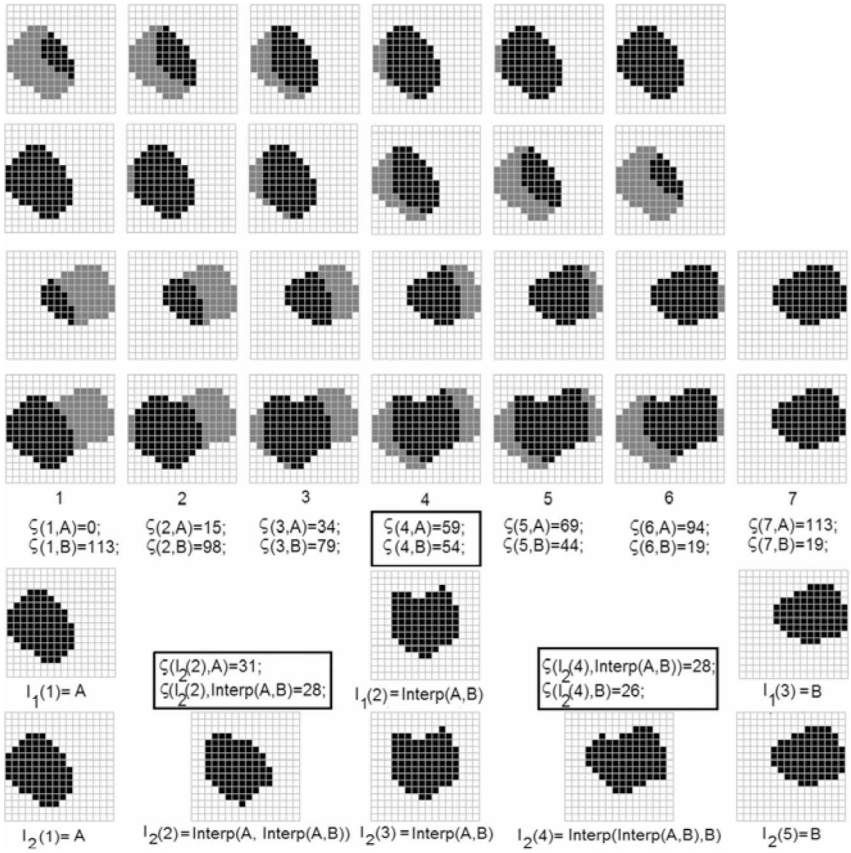

Fig. 3. Synthetic example of interpolation based on conditional dilation. Input shapes are from Fig. 2(a). In the first three rows, the current shape submitted to conditional dilation is in black; the rest of the reference shape is in gray. Row 1: dilatcond($A \cap B$; A; i) , $i = 1, \ldots, l_A$; $l_A = 6$; Row 2: dilatcond($A \cap B$; A; $l_A - i + 1$) Row 3: dilatcond($A \cap B$; B; j) , $j = 1, \ldots, l_B$; $l_B = 7$; Row 4: seq(A, B, i) , $i = 1, \ldots, max(l_A, l_B)$. Row 4 represents the logical OR of rows 2 and 3 and shows the transition sequence built with (5). The distances of each sequence element to input shapes are computed with (6). Rows 5 and 6 show the first two levels of the interpolation process.

as follows:

$$seq\,(A;B;i) = \begin{cases} \text{dilatcond}\,(A\cap B;A;l_A-i+1)\cup \\ \cup\text{dilatcond}(A\cap B;B;i), & \text{if } i \le \min\,(l_A,l_B) \\ \text{dilatcond}\,(A\cap B;B;i)\,, & \text{if } l_A \le i \le l_B \\ \text{dilatcond}\,(A\cap B;A;l_A)\,, & \text{if } l_B \le i \le l_A \end{cases} \quad \text{for } i = 1,\ldots,\max\,(l_A,l_B)\,. \tag{5}$$

The core of (5) is its first branch, which describes the integration of the parallel dilations in order to transform shape A into shape B. The second and third branches of (5) represent mutually exclusive alternatives, and are necessary in order to handle the difference in the l_A, l_B lengths of the two dilation processes that are combined.

The central idea behind this fusion approach is to create a smooth transition sequence from region A toward region B. An example of how a transition sequence is created is shown in Fig. 3. For a better visualization of the interpolation process, the input shapes in Fig. 3 are not aligned (much less iterations of conditional dilations are necessary for aligned 16×16 images).

The elements of the transition sequence $seq(A, B, i)$ exhibit a gradual change of shape from A to B. Therefore, the first elements are more similar to A, while the last ones are more similar to B. Our objective is to create a smooth change of shape between A and B via interpolation. Therefore, each iteration of the interpolation process selects one single element from the generated transition sequence, which will be further called the *median element*. Ideally, the median element should be equally similar to both input shapes; in practice, the equal similarity criterion is replaced by (6), which calculates the index i_{med} of the median element as

$$i_{\text{med}} = \underset{i=1,\ldots,\,\text{length}(seq(A,B))}{\arg\min} \left|\varsigma(seq(A,B,i);A) - \varsigma(seq(A,B,i);B)\right| \tag{6}$$

where ς denotes the distance between two shapes. The proposed approach computes the distance between two shapes as the cardinal of the symmetric difference of these two shapes as

$$\varsigma\,(S_1,S_2) = \text{card}\,(S_1 \Delta S_2)\,. \tag{7}$$

The design of the proposed interpolation scheme is hierarchical. At the first level, one transition sequence $seq(A, B)$ is created between input shapes A and B. Let $\text{Interp}(A,\ B) = seq(A,\ B,\ i_{\text{med}})$ be the median element of this transition sequence. The second level creates two transition sequences, namely seq(A, Interp(A, B)) and seq(Interp(A, B), B). At this level, one median element is created for each transition sequence

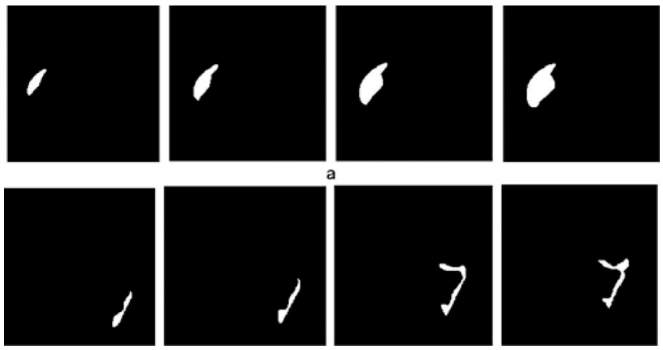

Fig. 4. Anisotropic (directional) region growth. (a) Sequence of equidistant liver slices growing towards right. (b) Sequence of equidistant scapula slices growing toward the upper side of image.

and added to the interpolation sequence. An n-level hierarchical process between A and B will create an interpolation sequence containing 2^{n-1} slices. The number of levels is selected depending on the desired interslice resolution after interpolation. A two-level interpolation process is shown in Fig. 3, along with distances computed between the interpolated shapes and the input shapes. These distances show that the proposed interpolation creates a uniform shape change between A and B.

A special case for interpolation is one where two input slices are identical; such a case may occur for cylindrical structures such as blood vessels. For this case, the median element is always chosen to be identical to both input shapes.

C. Shape Alignment

Shape alignment is necessary for handling cases where the planar position of anatomical structures shifts significantly between slices. Chatzis and Pittas [27], Cohen-Or *et al*. [32], and Lee and Wang [29] perform shape alignment by object centralization (i.e., matching centroids of corresponding regions). Lee and Wang [29] noted that concave regions having the centroid outside the region are not handled well by object centralization. We propose a new approach for shape alignment that is based on the observation that the evolution of corresponding shapes across sections is many cases anisotropic with respect to their centroids (see Fig. 4).

Given two binary shapes ima_1 and ima_2, our alignment approach computes the translation vector (t_x, t_y) that corresponds to the minimum shape displacement achieving maximum shape overlap as

$$(t_x, t_y) = \arg \min_{i,j} \left((t_i, t_j) \,\middle|\, \text{area}\left(\mathrm{ima}_{1\,t_t,t_j} \text{ and } \mathrm{ima}_2\right) = \max \right) \tag{8}$$

where $\mathrm{ima}_{1\,t_t,t_j}$ represents the translated version of ima_1 with displacement (t_i, t_j).

The minimum shape displacement is necessary to select one unique solution from the solution space verifying the maximum shape overlap criterion; large solution spaces are typically obtained for inclusion cases ($\mathrm{ima}_{1t} \subseteq \mathrm{ima}_2$). Moreover, the minimum displacement criterion aligns the boundary parts that remain quasi-unchanged, and therefore, is consistent with anisotropic region "growing" or "shrinking."

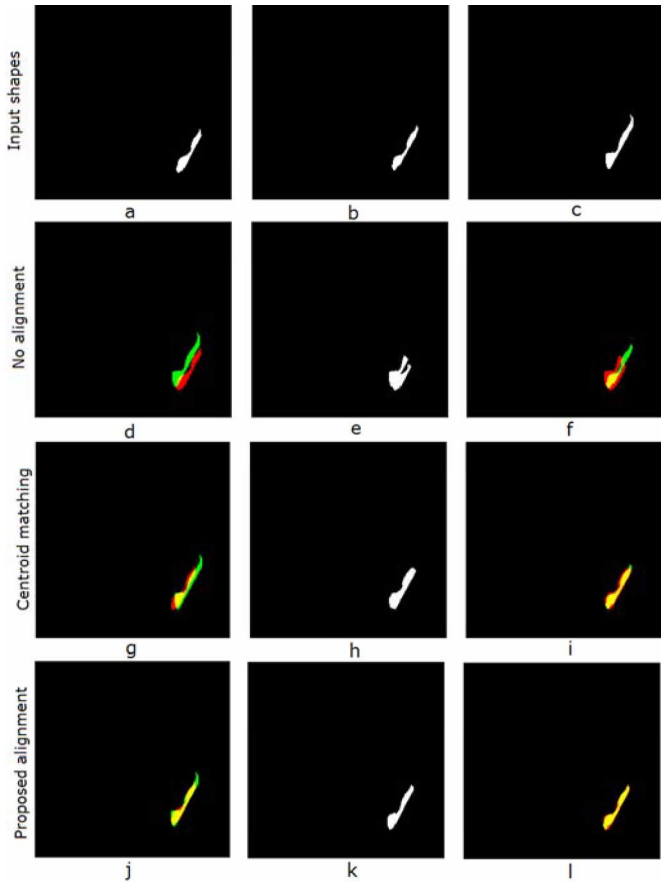

Fig. 5. First row: (a) and (c) Initial input shapes for interpolation. (b) "Ground truth" shape for interpolation evaluation. Second row: (d) Superposition of initial input shapes. (e) Interpolation without alignment. (f) Superposition of (e) with ground truth. Third row: (g) Superposition of input shapes aligned with centroid matching. (h) Interpolation of shapes in (g). (i) Superposition of (h) with ground truth. Fourth row: (j) Superposition of input shapes aligned with proposed method. (k) Interpolation of shapes in (j). (l) Superposition of (k) with ground truth. The color code for superposed images is yellow for common pixels, red and green for pixels belonging to one image only.

Prior to interpolation, both shapes are translated toward each other, namely $\mathrm{ima}_1 \xrightarrow{(t_x/2, t_y/2)} \mathrm{ima}_{1t}$ and $\mathrm{ima}_2 \xrightarrow{(-t_x/2, t_y/2)} \mathrm{ima}_{2t}$. The result of interpolation (i.e., the median element in the transition sequence) is already located at equal shifts from the input shapes and does not need a reverse translation. Fig. 5 shows a qualitative comparison of level one-interpolation results using the same two input shapes and two alignment techniques, as well as no alignment. For elongated, thin shapes, our proposed alignment yields better results than the centroid matching.

One limit of the proposed alignment approach is its high computational complexity. In practice, the search for the minimum shape displacement achieving maximum shape overlap can be constrained to relatively small rectangular windows, and performed via optimized maximum–minimum type searches. The choice of the window size depends on the interslice and intraslice resolution of the input data.

D. Branching

As shown in Fig. 1, branching handles the one-to-many correspondence approach. The main assumption behind branching is

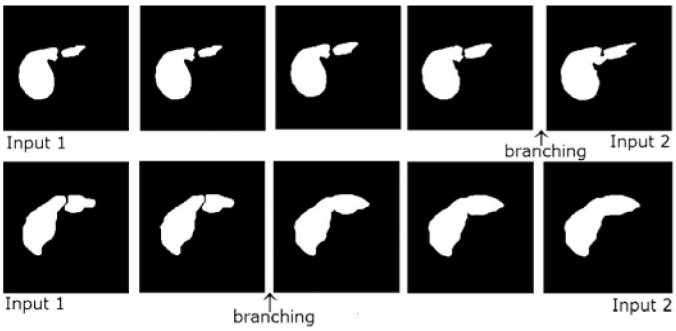

Fig. 6. Two examples of second-level interpolation sequences in branching cases. First row: the interpolated sequence contains only "branches"-type shapes. Second row: the interpolated sequence contains one "branches"-type and two "trunk"-type shapes.

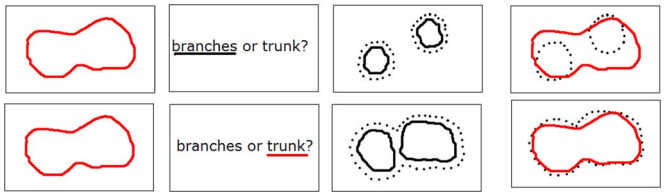

Fig. 7. Evaluation of the topology of the interpolated slice using dilation. First column: 'trunk'-type slice (in red). Second column: topology of the interpolated slice to be estimated. Third column: 'branches'-type slice (in black) and dilation of branches (dashed). Fourth column: overlap of first and third column.

that all "branches" overlap partially with the "trunk;" the limits of this assumption were discussed in Section II-A.

The proposed branching approach aims to generate a smooth transition between the topologies of the input slices without using a heuristic on where the change in topology should take place (for a heuristic-based branching algorithm, see [23]). At a given interpolation level, a median slice is created between two input slices in a one-to-many correspondence. This median slice may contain either a "trunk" or "branches," depending on the interslice topology correspondence. Since our interpolation approach is hierarchical, the change in topology (i.e., the branching phenomenon) may occur at a variable location in the interpolation sequence (see Fig. 6).

1) Estimating the Topology of the Interpolation Slice: Let us consider two input slices A and $B = \bigcup_{i=1}^{m} B_i, B_i \cap B_j = \Phi$ for $\forall i \neq j$ in a one-to-many correspondence at a given interpolation level. The decision on the topology of the median slice Interp(A, B) that will be the output of the interpolation process, considers the following two aspects of the "branches"–"trunk" correspondence.

1) The size of the union of "branches" relative to the size of the "trunk."
2) The spatial proximity of the "branches."

Both aspects can be simultaneously evaluated using morphological dilation, as shown in Fig. 7. In case the dilation of the union of the branches encompasses the trunk, it is reasonable to conclude that the branching occurs closer to the "branches" slice than to the "trunk" slice; therefore, the median interpolated slice should be a "trunk"-type. Conversely, if branches are either small-sized or wide apart, then one may conclude that the branching phenomenon occurs closer to the "trunk" slice than to the "branches" slice; therefore, the interpolated slice should be a "branches"-type. The mathematical formalism associated to the topology estimation is given by

$$\text{Interp}\,(A,B) = \begin{cases} \text{Interp}\left(A, \bigcup_{i=1}^{m} B_i \oplus K\right), & \text{if } A \subseteq \bigcup_{i=1}^{m} B_i \oplus K \\ \bigcup_{i=1}^{m} \text{Interp}\,(A_i, B_i), & \text{where } A = \bigcup_{i=1}^{m} A_i \text{ otherwise.} \end{cases} \tag{9}$$

The condition to be evaluated consists in whether shape A is included or not in the union set of the dilated "branches." In case this inclusion is true, then the median shape will be of "trunk"-type (i.e., will contain one single connected region, thus will have the same topology as shape A). Otherwise, the median shape will be "branches"-type and have the same topology as shape B (m branches); the median shape will be built as a union of m one-to-one interpolation processes between A_i (subregions of A) and branches B_i. The splitting of A into subregions is discussed in the following section.

The size of the structuring element plays a significant role in the topology evaluation process. The selection of the structuring element must be done according to the interslice resolution of the input data.

2) Splitting the "Trunk" Into Subsections: The idea is to divide the "trunk" into nonoverlapping subregions for a pairwise interslice correspondence with the "branches." This "splitting" process allows for further applying the interpolation method described in subsection A for the newly created pairs of corresponding regions.

As a simple example involving two "branches," let us consider the following 2-D binary shapes: A located in slice i, and B_1, B_2 located in slice $i+1$. Assuming that the median shape is "branches"-like, A must be partitioned into two shapes, A_1 and A_2. Therefore, a one-to-many correspondence case $(A; B_1, B_2)$ is to be transformed into two one-to-one correspondence cases, namely $(A_1; B_1)$ and $(A_2; B_2)$.

Considering a one-to-one correspondence between two regions in adjacent slices, these two regions feature some degree of similarity for a reasonable slice thickness. Consequently, if a "branching" interslice correspondence is to be transformed into a set of one-to-one correspondences, then the "splitting" process has to create a partition consisting of regions similar in shape with the corresponding "branches." One solution for splitting would be to use a marker-controlled watershed approach. However, this approach is likely to fail to "split" correctly the trunk in cases where the shape of the trunk does not conserve many details about the shape of the branches (as shown, for instance, in the first row of Fig. 7).

The proposed splitting approach consists of an iterative algorithm based on conditional dilation, which allows for creating a partition featuring interslice shape similarity. The main steps of the algorithm are as follows.

1) Initialization. Given the 2-D binary regions B_1, B_2, $\ldots$, B_m in branching correspondence with A, and under

the assumption of partial overlap, the following intersections are computed: $\mathrm{Int}_i = B_i \cap A, i = 1, \ldots, m$.

2) *Region "splitting" based on conditional dilation*. The binary regions $\mathrm{Int}_i,\ i = 1, \ldots, m$ represent seed regions that are simultaneously submitted to iterative conditional dilations with respect to the four-connectivity structuring element K, and to a reference region. This reference is changing with each iteration, and it is specific to every dilated binary region. To describe the iterative process, let us first consider the following notations and definitions:

1) $S_i^l i = 1, \ldots, m$ are the m binary regions evolving with each iteration, and l is the index of the iteration. From the initialization phase, $S_i^0 = \mathrm{Int}_i,) i = 1, \ldots, m$.
2) $\mathrm{Ref}_i^l = \mathrm{comp}\left(S_1^l\right) \cup \ldots \cup \mathrm{comp}\left(S_{i-1}^l\right) \cup \mathrm{comp}\left(S_{i+1}^l\right) \cup \ldots \cup \mathrm{comp}\left(S_m^l\right)$ is the reference region for the region S_i^l at iteration l. The comp (S_*^*) operator computes the relative complement of set S_*^* in A. It is easy to prove that$(\forall)\, i,\ l,\ S_i^l \subset A$, thus the complement set operation is valid.

This recursive definition of the reference region for conditional dilation allows for the simultaneous expansion of the seed regions inside A while preventing the occurrence of overlaps during expansion.

Using previously defined notations, the partition of A into m nonoverlapping regions is described by the equations

$$S_i^{l+1} = S_i^l \oplus_{\mathrm{Ref}_i^l} K,\ S_i^0 = \mathrm{Int_i},\ i = 1, \ldots, m \qquad (10)$$

where l is the index of the iteration and K is the four-connectivity structuring element.

The convergence of this iterative process is reached within a number p of iterations. The final "split" of A into m distinct and nonoverlapping regions is achieved at convergence as

$$S_i^p = A_i, \qquad i = 1, \ldots, m; \qquad A = \bigcup_{i=1}^{m} A_i. \qquad (11)$$

The frontiers between the nonoverlapping regions are built gradually during the iterative splitting process. For instance, if one pixel corresponding to the dilation of region A_i belongs already to another region A_j, then this pixel will belong to the frontier between regions A_i and A_i.

Fig. 8 illustrates the iterative process of "splitting" based on conditional dilation, as well as the transformation of the "branching" correspondence into two simple one-to-one correspondences, which will be handled by the interpolation approach presented in Section II-B. One should note that branching evaluation and branching correspondence are performed at each iteration of the hierarchical interpolation algorithm if a one-to-many correspondence case occurs.

E. Extrapolation

Due to the finite interslice resolution, the acquisition process does not provide information about the real extremities of the anatomical structures. Consequently, the *extreme* 2-D regions in the serial sequence representing a 3-D object feature a one-sided correspondence. To generate a smooth surface closing for branches along the z-direction, an extrapolation technique based on the conditional dilation is proposed. For this purpose, it is assumed that the real extreme regions of the anatomical structures are one pixel-sized; these will be further called *extreme points*.

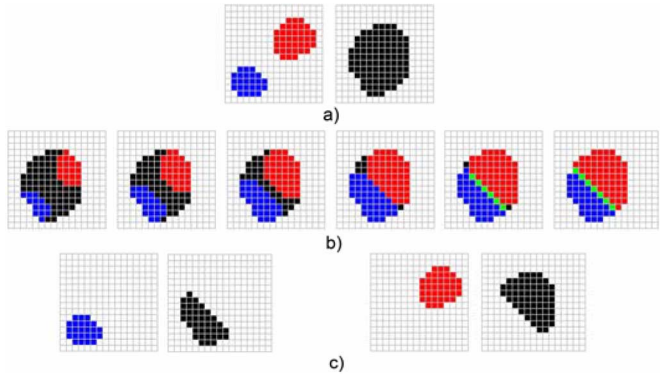

Fig. 8. Example of iterative "splitting." (a) Initial "branching" interslice correspondence. (b) Iterative "splitting" process based on conditional dilation-frontier generation is shown in green. (c) Final interslice correspondence after "splitting."

The extreme point P is virtually located in the input slice which does not contain E (i.e., the extreme region), and is chosen as the center of mass of E. This simple choice enables us to handle extreme regions caused by "appearances" as well as "disappearances" of branches. A more elaborate choice would need to take into consideration the trajectory of all centers of mass in the particular branch to be closed. Future work will address this issue, which does not have a trivial implementation for "appearances" of new regions.

The extrapolation process is therefore implemented as a one-to-one correspondence case between the extreme region E and corresponding extreme point P. Equation (5) can be adapted for extrapolation as

$$\mathrm{seq_{ext}}\,(E; P) = \mathrm{dilatcond}\,(P; E; l_P)\,, \qquad i = 1, \ldots, l_P \qquad (12)$$

where l_P is the number of iterative conditional dilations necessary to generate the extreme region E from P. From this sequence, the median element is chosen according to (6) and represents the output of the extrapolation process. One should note that, as opposed to interpolation, extrapolation is not iterative. Interslice region correspondence is evaluated at each iteration of the interpolation process, and extrapolation deals with zero-to-one correspondence cases if those occur.

III. Experimental Results

For quantitative performance evaluation purposes, our interpolation algorithm was compared with the approach recently proposed by Jeong and Radke in [24]. Their approach was chosen as reference for the comparative performance analysis since it serves the same purpose of interslice shape-based interpolation of anatomical structures. A brief description of their algorithm is given in Section III-A, while Section III-B contains the comparative performance analysis. Section III-C and Section III-D discuss the results obtained by branching and extrapolation algorithms. Table I summarizes information about the experimental datasets involved in the validation.

TABLE I
SUMMARY OF CHARACTERISTICS OF EXPERIMENTAL DATASETS

Anatomical structure	Image type	Size of sequence= =size(slice) x no. of slices	Voxel size (*sx* x *sy* x *sz*) (mm^3)
1. Liver	CT	180x180x97	1.25x1.25x2
2. Liver	CT	189x189x74	1.25x1.25x2
3. Liver	CT	187x187x51	1.25x1.25x2
4. Scapula	MRI	256x256x34	1.25x1.25x7
5. Scapula	MRI	256x256x54	1.25x1.25x7
6. Scapula	MRI	256x256x39	1.25x1.25x7

A. Interpolation Using Elliptical Fourier Descriptors [24]

EFDs were first introduced by Kuhl and Giardina [33]. They are suitable for biological shape representation and modeling due to the absence of sharp edges in such shapes.

Given an input sequence of parallel slices, the approach in [24] performs the interslice interpolation by interpolating the EFDs belonging to corresponding closed contours located in adjacent slices. In a first step, the EFD harmonic sets of the corresponding contours are extracted via forward Fourier analysis. Each harmonic in the EFD set is interpolated using a cubic spline interpolant. Finally, slices at z locations in-between input slices are computed from interpolated EFD coefficients using reverse Fourier analysis. Jeong and Radke [24] state that the ability of EFDs to accurately represent shape contours depends on the number of coefficients used for approximation; they found that $N = 8$ harmonics is optimal for both biomedical and simulated shape interpolation.

Our implementation of the EFD-based interpolation uses N=8 harmonics as well. The differences between our implementation of the algorithm in [24] and the original one are outlined as follows.

1) We used a different contour parameterization technique. The contour parameterization in [24] works well only for convex shapes. Our database contains convex as well as concave shapes; in the latter case, the center of mass may fall outside the concave shape, and the radius that unites the center of mass with boundary points may have multiple intersections with the contour. The contour parameterization in our implementation is based on a chain generation using a simple contour following technique. A similar parameterization has been used in Ballaro *et al*. [34] for extracting EFD coefficients.
2) Since our input data are represented by connected regions, the contours of these regions consist of connected points. Hence, there is no need for interpolating between contour points prior to the generation of the EFD coefficients from input slices.
3) The approach in [24] deals only with the one-to-one correspondence case; all their sequences (both synthetic and medical) exhibit one contour per slice only. Thus, interslice correspondence was performed with the method in Section II-A.
4) EFD interpolation was constrained to the currently analyzed pair of input contours; therefore, a linear interpolation instead of a cubic spline one was used.

B. Comparative Performance Analysis

The interpolation approach proposed in this paper was compared with the reference algorithm described in Section III-A. Input data for both methods consisted of sets of uniformly subsampled sets of CT and MR images. Due to the low interslice resolution of the input MR data relative to CT, subsampling is performed differently on CT and MR sets, as described later.

1) *CT data*. Let $P_i, P_{i+1}, P_{i+2}, P_{i+3}, P_{i+4}$ be a subsequence of input CT slices; from this subsequence, the input slices for the validation test are P_i and P_{i+4}.
   The proposed approach and the reference algorithm produce interpolated slices $\hat{P}_{i+1}, \hat{P}_{i+2}, \hat{P}_{i+3}$ that are compared with the corresponding real slices. Our interpolation algorithm generates three intermediate slices in two iterations. The first one produces one median slice $\hat{P}_{i+2}$ between P_i and P_{i+4}, while the second iteration produces two median slices, namely $\hat{P}_{i+1}$ from (P_i, $\hat{P}_{i+2}$) and $\hat{P}_{i+3}$ from ($\hat{P}_{i+2}, P_{i+4}$). The EFD interpolation algorithm is noniterative, generating all three slices from interpolated EFD coefficients at equally spaced z-levels between the two input locations.
2) *MR data*. Considering the low interslice resolution of the MR datasets, subsampling is performed on MR data by eliminating only one slice instead of three. Let P_i, P_{i+1}, P_{i+2} be a subsequence of input MR slices; from this subsequence, the input slices are P_i and P_{i+2}. The proposed approach and the EFD interpolation algorithm produce the interpolated slice $\hat{P}_{i+1}$ that is compared with P_{i+1}.

For both data types, two versions of the proposed approach were implemented using two structuring elements of different shape and size as follows: 1) a flat diamond-shaped structuring element of radius 1 (SE_1); 2) a circular-shaped structuring element of radius 4 (SE_2).

The first measure that was used to compare the two interpolation algorithms consists of an overlap-based error measure computed as the ratio of the wrongly estimated pixels with respect to the area of the reference slice given by

$$\varepsilon(P, \hat{P}) = \mathrm{card}(P \Delta \hat{P}) / \mathrm{card}(P) \tag{13}$$

where P and $\hat{P}$ are sets corresponding to the reference and interpolated binary slices, Δ is the symmetric difference, and card is the cardinal function.

Tables II and III contain error values obtained from the evaluation of the results obtained by interpolating slices between input data generated by subsampling the CT and MR datasets, respectively.

As shown by data in Tables II and III, our approach outperforms the EFD interpolation for two liver datasets (CT-1 and CT-3), and for two scapula datasets (MR-1 and MR-3). For CT-2 and MR-2, the EFD interpolation performs slightly better than our algorithm, although average error rates remain comparable. The higher error rates obtained in the scapula MR datasets by both interpolation approaches is due to the sensitivity of the

TABLE II
RESULTS OBTAINED BY PROPOSED APPROACH AND BY REFERENCE ALGORITHM FOR CT DATASETS

Dataset	Input slices for interpolation	Slice index and area of slice (in pixels)	ε for proposed interpolation (SE_1)	ε for proposed interpolation (SE_2)	ε for EFD interpolation
CT-1	#13, #17	#14– 3372 pixels	4.48%	4.12%	5.31%
		#15 – 3732 pixels	5.36%	6.86%	5.89%
		#16- 3854 pixels	5.53%	4.64%	6.15%
	#58, #62	#59- 5661 pixels	5.21%	3.37%	5.46%
		#60- 5569 pixels	3.91%	6.48%	5.28%
		#61- 5484 pixels	2.75%	2.9%	5.18%
	Average for CT-1 dataset		**8.70%**	**10.14%**	**10.8%**
CT-2	#37, #41	#38-5570 pixels	7.32%	4.11%	6.18%
		#39-5431 pixels	11.78%	5.36%	5.79%
		#40-5382 pixels	11.25%	7.79%	5.25%
	#17, #21	#18-4656 pixels	9.12%	8.98%	8.07%
		#19-4740 pixels	12.8%	12.34%	10.18%
		#20-5241 pixels	12.47%	13.34%	8.21%
	Average for CT-2 dataset		**14.97%**	**14.95%**	**12.13%**
CT-3	#13, #17	#14- 3705 pixels	8.56%	11.17%	10.26%
		#15- 3664 pixels	6.80%	7.21%	9.96%
		#16- 3951 pixels	7.31%	7.85%	8.68%
	#21, #25	#22- 5096 pixels	4.1%	5.02%	5.71%
		#23- 5004 pixels	6.02%	6.24%	7.05%
		#24- 5098 pixels	3.9%	3.33%	6.65%
	Average for CT-3 dataset		**7.42%**	**7.49%**	**7.50%**

TABLE III
RESULTS OBTAINED BY PROPOSED APPROACH AND BY REFERENCE ALGORITHM FOR MR DATASETS

Dataset	Index of input slices for interpolation	Slice index and area of slice from input data (in pixels)	ε for proposed interpolation (SE_1)	ε for proposed interpolation (SE_2)	ε for EFD interpolation
MR-1	#11, #13	#12-996 pixels	17.47%	21.38%	31.02%
	#17, #19	#18-692 pixels	12.72%	15.03%	42.34%
	Average for MR-1 dataset		**28.24%**	**30.95%**	**40.21%**
MR-2	#19, #21	#20-486 pixels	19.14%	21.81%	23.46%
	#27, #29	#28-268 pixels	17.53%	16.79%	16.79%
	Average for MR-2 dataset		**22.65%**	**24.46%**	**26.24%**
MR-3	#15, #17	#16-775 pixels	11.22%	13.29%	17.29%
	#23, #25	#24-420 pixels	7.12%	7.89%	26.90%
	Average for MR-3 dataset		**10.36%**	**10.51%**	**28.59%**

error measure in the area of the reference region. For this reason, the area of the reference slice is given in the third column of Tables II and III. One may note that scapula slices can be ten times smaller in size than liver slices, which impacts significantly on ε.

Fig. 9 shows two examples of interpolation results obtained by our algorithm (with two different structuring elements SE1 and SE2), and by EFD interpolation. The error values for both interpolation processes are available in Tables II (second row of CT-1) and Tables III (first row of MR-3), respectively. For an easy visualization of the quality of interpolation, a color-coded overlap of interpolated slices with the corresponding reference ones is shown as well. One may note that, for MR scapula slices, the interpolation is of reasonable quality for both interpolation algorithms, although the corresponding errors in Table III are relatively high.

As shown in Tables II, III, and in Fig. 9, the proposed interpolation algorithm yields similar performances for

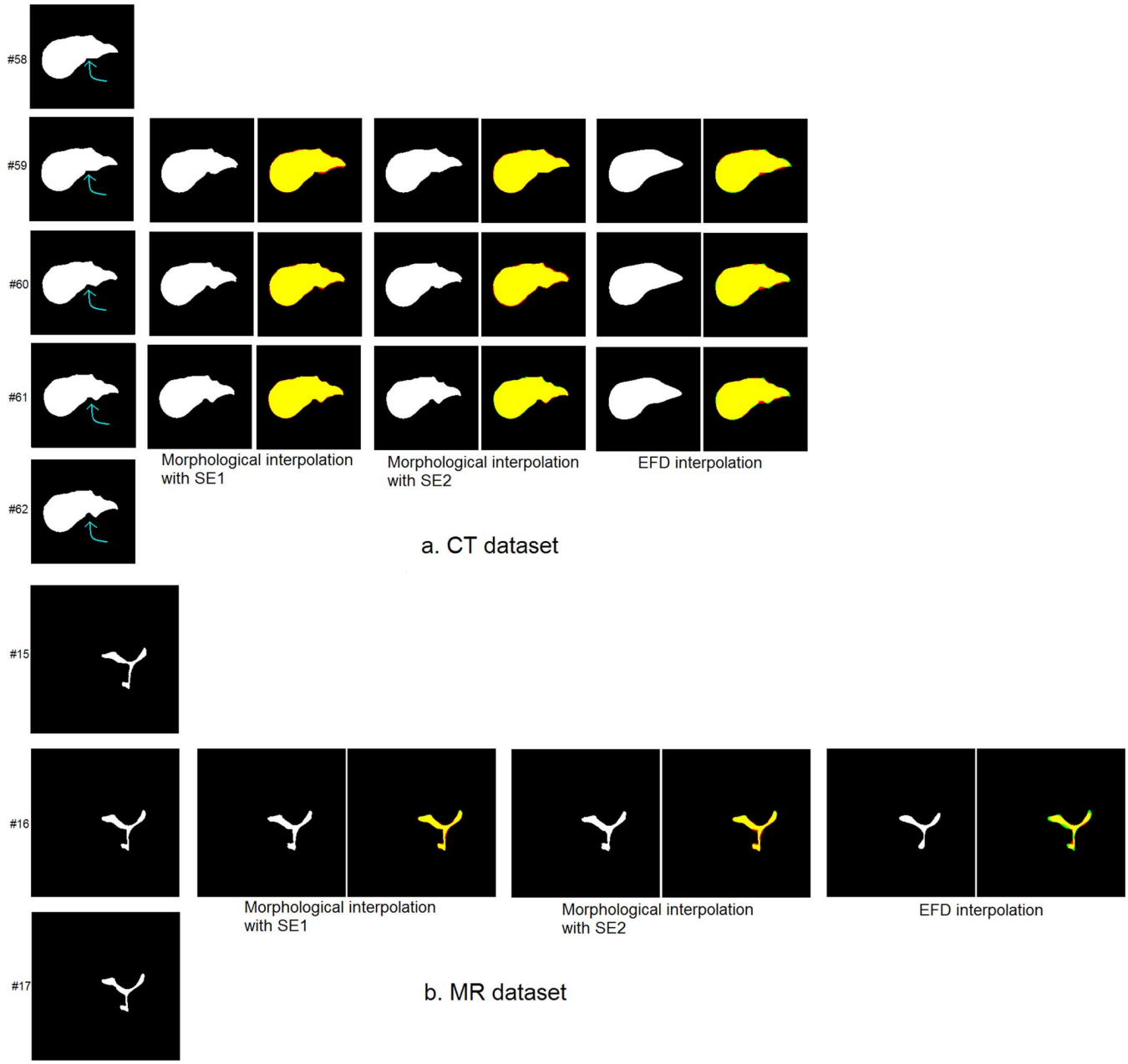

Fig. 9. (a) Interpolation of three slices between input slices # 58 and 62 in the CT-1 dataset. (b) Interpolation of one slice between input slices # 15 and 17 in the MR-3 dataset. First column: input and reference slices; columns 3, 5, and 7 show a color-coded overlap of interpolated slices with the corresponding reference ones (yellow: common pixels, red: pixels belonging to interpolated slice only, green: pixels belonging to reference slice only).

two structuring elements of different size and shape. This suggests a relative invariance of our approach to the size and shape of the used structuring element; future work will make further investigations in this area.

The visual inspection of interpolated slices shown in Fig. 9 reveals the fact that, although the error statistics are close for our algorithm and for the EFD interpolation, the EFD interpolated slices have a significantly different appearance from the reference ones. Specifically, the EFD interpolation produces slices that are much smoother than the corresponding reference slices. For instance, the blue arrows in the first column of Fig. 9 show a local shape concavity that deepens throughout the input sequence. Both versions of our algorithm capture the evolution of this local detail, while the local concavity is not present at all in the interpolated EFD slices.

The oversmoothed appearance of slices interpolated with the EFD interpolation algorithm characterizes all results produced on the CT and MR datasets. The oversmoothing phenomenon is not desirable for medical applications such as morphometry, 3-D therapy planning, etc., where local shape details matter significantly. On the other hand, our proposed approach produces slices that have similar smoothness as the reference ones, and capture well local shape characteristics such as concavities and protrusions. Figs. 10 and 11 illustrate the oversmoothing that is characteristic to EFD interpolation, as well as the conservation of local shape details using our proposed approach.

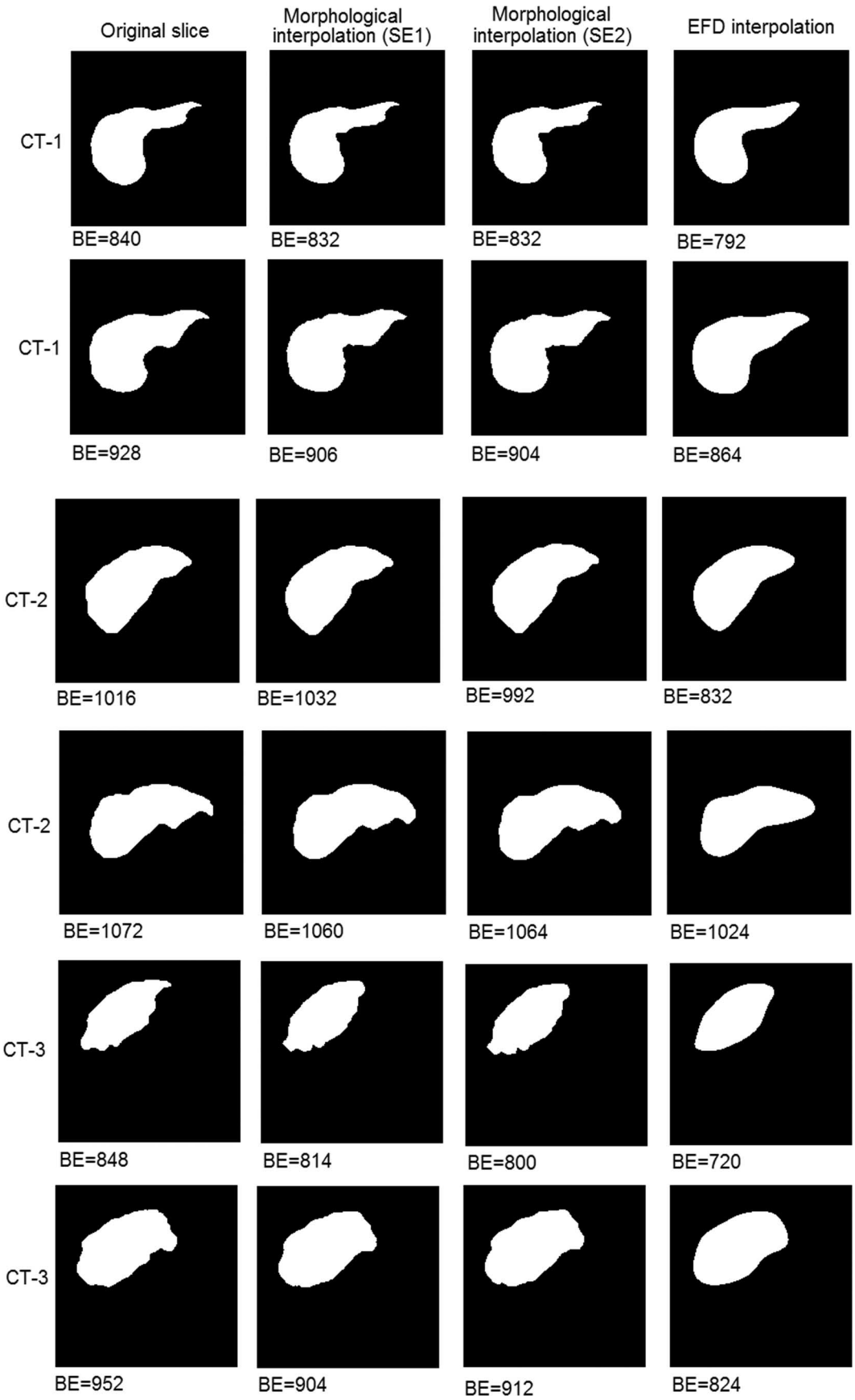

Fig. 10. Smoothness comparison of reference slices and interpolation results for CT images. Two examples from each CT dataset are shown.

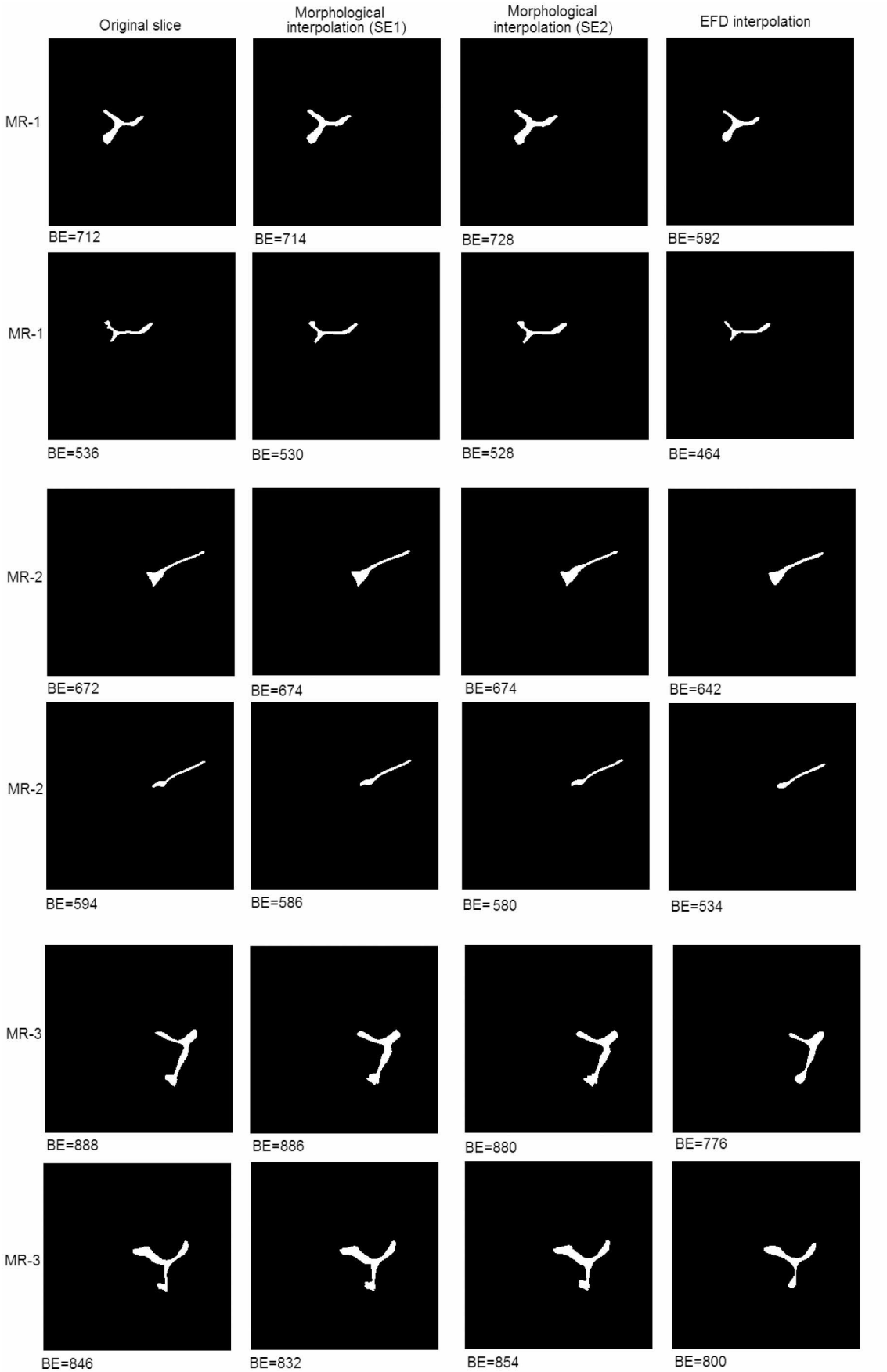

Fig. 11. Smoothness comparison of reference slices and interpolation results for MR images. Two examples from each MR dataset are shown.

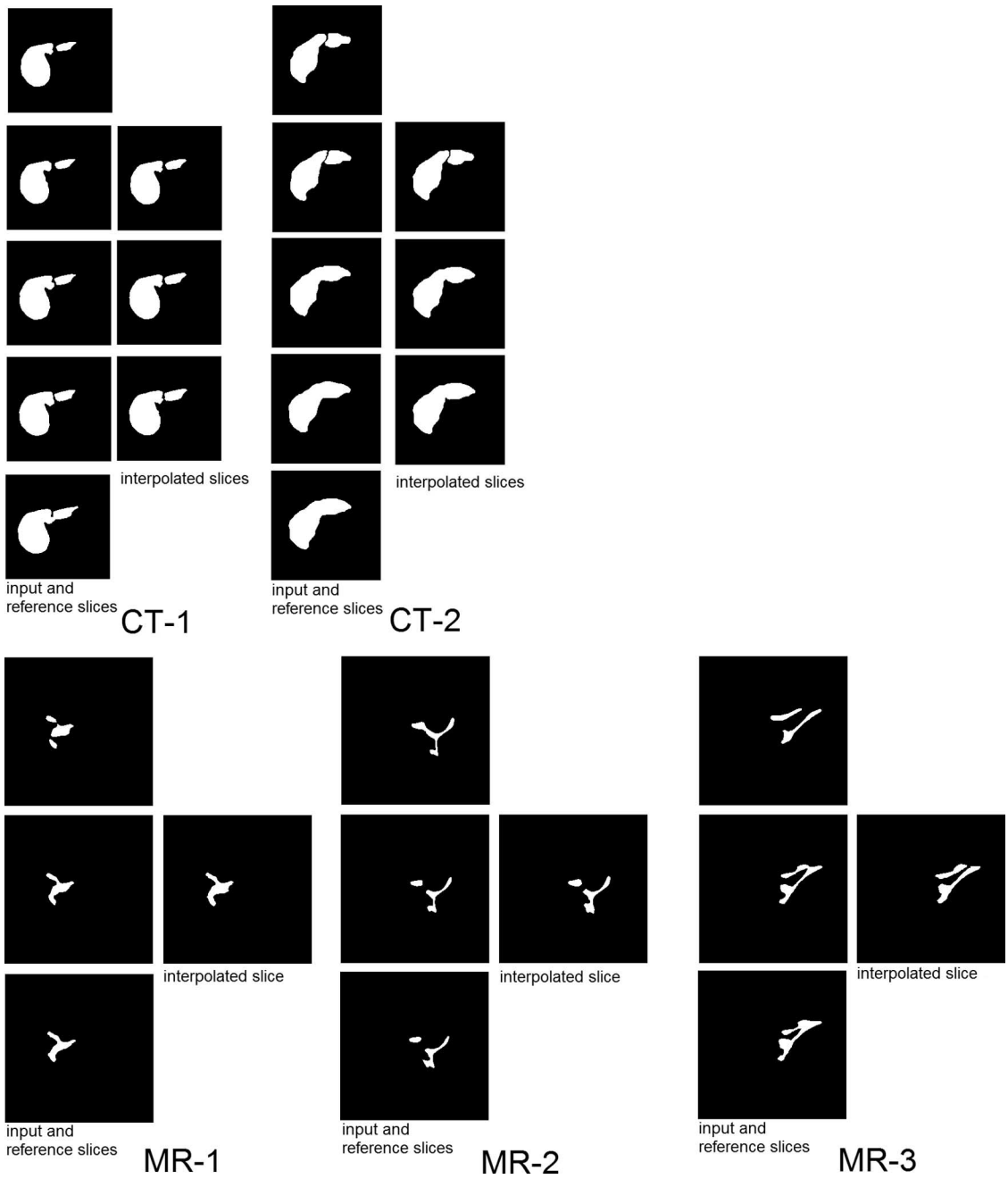

Fig. 12. Branching cases in CT-type (upper row) and MR-type (lower row) sequences.

The quantification of oversmoothing was performed with the bending energy metric. The bending energy is obtained by integrating the square curvature along the contour as

$$BE = \sum_{k=1}^{N} c^2(k) \tag{14}$$

where N is the number of points in the contour and $c(k)$ is the Freeman code corresponding to point k. At a given scale, the smoother the contour, the lower its bending energy is. As pointed out by Delingette [35], the bending energy cannot be used in general as a smoothness measure, since it is not scale invariant. As shown in Tables II and III, all interpolated and reference shapes have similar sizes, therefore their bending energy is directly comparable and can be used as a smoothness measure in the context of this study. However, no statistics can be computed over a dataset of variable-sized shapes, since the difference in bending energies of interpolated and reference shapes is size-dependent, too. For the purpose of comparison between different interpolated versions of the same shape, bending energies are shown for each shape in Figs. 10 and 11. One may notice that the bending energy of EFD interpolation results is consistently lower than the bending energy of the initial shape. Moreover, the bending energy of results obtained with our proposed approach is most of the times comparable to the bending energy of the initial shape. Finally, the bending energy is a global

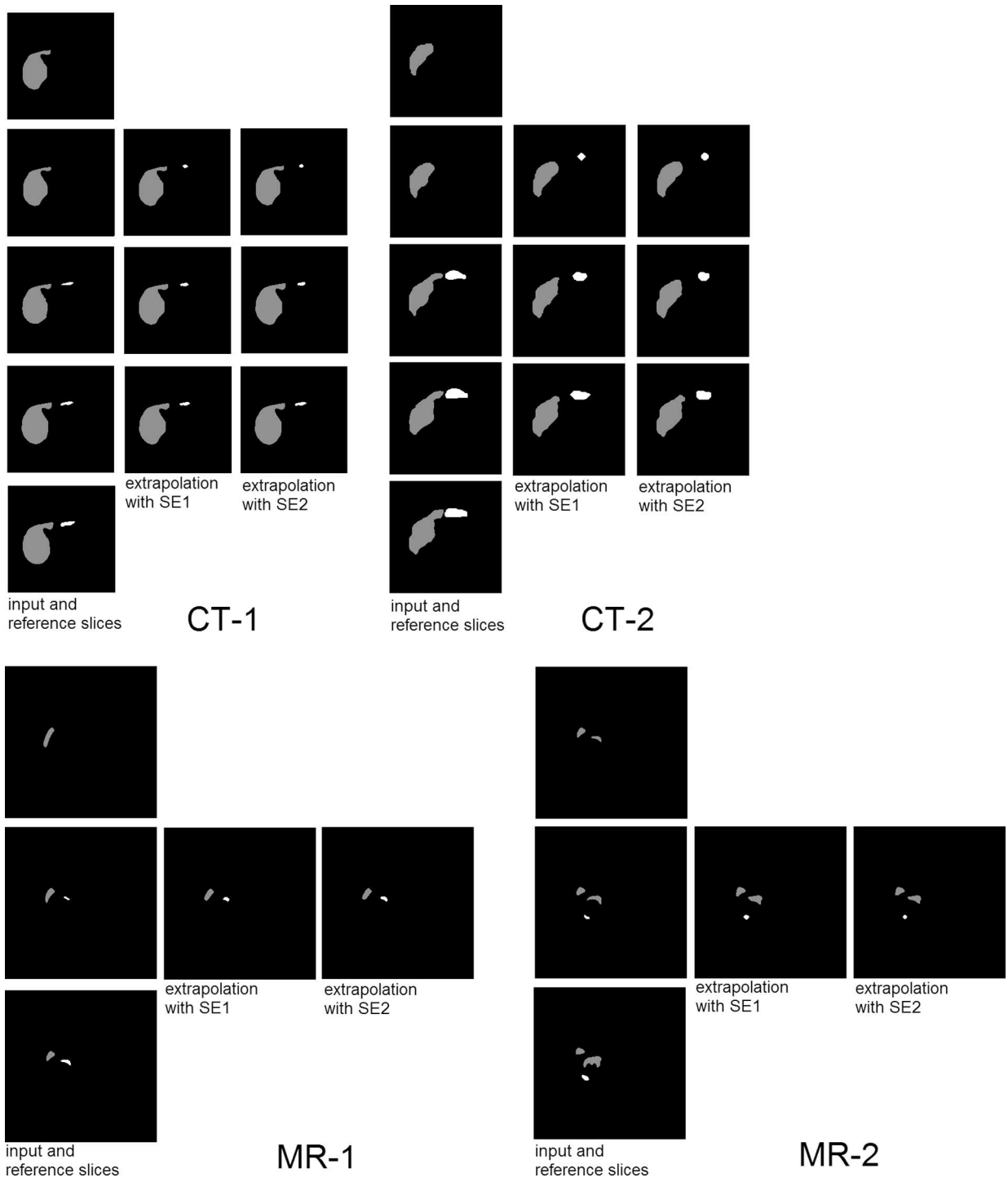

Fig. 13. Extrapolation results for 2 extreme regions in CT data (upper row) and 2 extreme regions in MR data (lower row). Nonextreme regions are grayed out.

shape descriptor, therefore it does not capture information about whether interpolated shapes replicate local shape details (concavities, protrusions) of reference shapes or not. Figs. 9–11 provide qualitative evidence on this aspect.

C. Branching and Topology Preservation

The proposed branching approach (described in Section II-D) creates either a "trunk"- or a "branches"-type intermediate slice between two input slices in a one-to-many correspondence. The decision on the topology of the interpolated slice considers the relative size and position of the "branches" with respect to the "trunk." This section assesses whether the topology of sections interpolated between input slices in a one-to-many correspondence is correct with respect to the reference slices.

Our entire database contains one branching case per dataset with the exception of CT-3 that contains no branching. Fig. 12 shows a comparison between the topology of interpolated slices

and the reference ones for all the branching cases in our database. The input slices for interpolation are also shown as contextual information.

Due to the different interslice resolution of CT and MR datasets, the structuring element used for estimating the topology of the interpolated slice ("trunk"- or a "branches"-type) is different for CT and MR-slices; specifically, a flat diamond-shaped structuring element of radius 1 (SE_1) was used for CT datasets, and a circular-shaped structuring element of radius 4 (SE_2) was used for MR datasets. Regarding interpolation, only results obtained with SE_1 are shown for simplicity, since the topology of the slices interpolated with SE_1 and SE_2 stays the same. As shown in Fig. 12, our approach preserves the topology of the reference slices in four branching cases out of five. The branching case where the estimated slice is "branches"-type while its corresponding reference is "trunk"-type occurs in the MR-3 sequence. This error is probably caused by the fact that, in the reference slice, the "trunk" consists of two branches united by a relatively narrow bridge, whose presence was not estimated by our approach.

D. Extrapolation

The results obtained for extreme region extrapolation for branches were inspected using two criteria, namely: 1) the topology of the slice containing the extrapolated region and 2) the shape of the extrapolated region versus the corresponding reference shape. Examples of extrapolations performed on CT and MR images are shown in Fig. 13.

Error statistics were not computed for extrapolation, since the small size of extrapolated and extreme regions would bias the results. From the visual inspection of the examples in Fig. 13, one may note that the topology of the reference slices is not always preserved by extrapolation (see second row for CT slices). Specifically, extrapolation may introduce a small region where it does not exist. It is, however, believed that this limit is outweighed by the advantage of generating smooth closings for branches. Some size and shape variability can be noticed between the extrapolated slices and the reference ones. Finally, for small-sized extreme regions, both structuring elements used for conditional dilation yield similar, good results; this is not true for larger sized extreme regions.

IV. Conclusion

This paper describes a new morphology-based approach for the interslice interpolation of segmented anatomical structures from volumetric images. Our approach handles explicitly interslice topology changes by decomposing a many-to-many correspondence into three fundamental cases: one-to-one, one-to-many, and zero-to-one correspondences. The only assumption underlying the proposed technique is the partial overlap between corresponding slices.

Prior to interslice interpolation between corresponding regions, an alignment based on the minimal displacement that achieves maximal interregion overlap is performed. It is shown that this new alignment method yields better interpolation results than the commonly used centroid matching [27], [29], [32].

Our interpolation approach is based on one morphological operator, namely conditional dilation. This differentiates our method from other existing morphological methods [28], [29], who use a combination of dilations and erosions. The transition sequence between two corresponding shapes in adjacent slices is obtained by integrating two parallel conditional dilations. When interpolating "branch"-type slices, the one-to-many correspondence (branching) is decomposed into several one-to-one correspondences by using an approach based on conditional dilation. Finally, for nonexistent correspondences ("extreme") slices, a smooth closing is achieved using a conditional dilation process as well.

The proposed interpolation process is iterative. One iteration of this process computes a transition sequence between a pair of corresponding input slices and selects the element equally similar to the input slices. This algorithmic design yields a gradual, smooth change of shape between the input slices. Therefore, the main contribution of our approach is its ability to interpolate between two shapes by creating a smooth, gradual change of shape, and without generating oversmoothed interpolated shapes. This contribution is supported by the experimental results shown in Section III. It is believed that the ability to create interpolated shapes of similar smoothness with the input is relevant for various medical applications such as 3-D morphometry and therapy planning where the preservation of local shape details matters.

Future work consists in extending of the proposed interslice interpolation method at a subpixel level, which will probably improve the results obtained for thin structures. This study will be based on the subpixel morphological operators introduced by Chen *et al*. [36].

Acknowledgment

The authors would like to thank L. Hebert, C. Moisan, M. Dufour (Department of Radiology, Laval University, QC) and H. Moffet (Department of Physical Rehabilitation, Laval University, QC) for providing the MR experimental database. The CT image sequences are courtesy of the Department of Radiology, University of Georgetown, US.

References

[1] R. T. Whitaker, "A level-set approach to image blending," *IEEE Trans. Image Process.*, vol. 9, no. 11, pp. 1849–1861, Nov. 2000.
[2] G. Barequet and A. Vaxman, "Nonlinear interpolation between slices," in *Proc. 3rd ACM Symp. Solid Phys. Model. (SPM)*, Beijing, 2007, pp. 97–107.
[3] M. Alexa, "Recent advances in mesh morphing," *Comp. Graph. Forum*, vol. 21, no. 2, pp. 173–196, 2002.
[4] S. Fang, R. Srinivasan, R. Raghavan, and J. T. Richtsmeier, "Volume morphing and rendering—An integrated approach," *Comput. Aided Geom. Des.*, vol. 17, no. 1, pp. 59–81, Jan. 2000.
[5] O. Nilsson, D. Breen, and K. Museth, "Surface reconstruction via contour metamorphosis: An Eulerian approach with Lagrangian particle tracking," in *Proc. IEEE Vis.* Oct. 23–28, 2005, pp. 407–414.
[6] H. Yang and B. Juttler, "3-D shape metamorphosis based on T-spline level sets," *Vis., Comput.*, vol. 23, no. 12, pp. 1015–1025, Dec. 2007.
[7] G. Turk and J. F. O'Brien, "Shape transformation using variational implicit functions," in *Proc. SIGGRAPH*, 1999, pp. 335–342.
[8] W. K. Pratt, *Digital Image Processing*. New York: Wiley, 1991.
[9] S. M. Goldwasser, R. A. Reynolds, D. A. Talton, and E. S. Walsh, "Techniques for the rapid display and manipulation of 3-D biomedical data," *Comput. Med. Imag. Graph.*, vol. 12, no. 1, pp. 1–24, 1998.

[10] E. H. W. Meijering, "Spline interpolation in medical imaging: Comparison with other convolution-based approaches," in *Proc. 10th Eur. Conf. Signal Process.*, 2000, vol. 4, pp. 1989–1996.
[11] S. P. Raya and J. K. Udupa, "Shape-based interpolation of multidimensional objects," *IEEE Trans. Med. Imag.*, vol. 9, no. 1, pp. 32–42, Mar. 1990.
[12] G. P. Penney, J. A. Schnabel, D. Rueckert, M. A. Viergever, and W. J. Niessen, "Registration-based interpolation," *IEEE Trans. Med. Imag.*, vol. 23, no. 7, pp. 922–926, Jul. 2004.
[13] G. J. Grevera and J. K. Udupa, "An objective comparison of 3-D image interpolation methods," *IEEE Trans. Med. Imag.*, vol. 17, no. 4, pp. 642–652, Aug. 1998.
[14] P. N. Werahera, G. J. Miller, G. D. Taylor, T. Brubaker, F. Daneshgari, and E.D. Crawford, "A 3-D reconstruction algorithm for interpolation and extrapolation of planar cross sectional data," *IEEE Trans. Med. Imag.*, vol. 14, no. 12, pp. 765–771, Dec. 1995.
[15] P. K. Saha, Y. Zhuge, and J. K. Udupa, "Fuzzy shape-based interpolation," in *Proc. SPIE Med. Imag.*, 2007, vol. 6512, pp. 65123W-1–65123W-10.
[16] T.-Y. Lee and C.-H. Lin, "Feature-guided shape-based interpolation," *IEEE Trans. Med. Imag.*, vol. 21, no. 12, pp. 1479–1489, Dec. 2002.
[17] G. M. Treece, R. Prager, A. Gee, and L. Berman, "Surface interpolation from sparse cross-sections using region correspondence," *IEEE Trans. Med. Imag.*, vol. 19, no. 11, pp. 1106–1114, Nov. 2000.
[18] G. M. Treece, R. Prager, A. Gee, and L. Berman, "Fast surface and volume estimation from non-parallel cross-sections for freehand 3-D ultrasound," *Med. Image Anal.*, vol. 3, no. 2, pp. 141–173, 1999.
[19] S. Morigi and F. Sgallari, "3-D long bone reconstruction based on level sets," *Comput. Med. Imag. Graph.*, vol. 28, pp. 377–390, 2004.
[20] A. Souza, J. K. Udupa, and P. K. Saha, "Volume rendering in the presence of partial volume effects," *IEEE Trans. Med. Imag.*, vol. 24, no. 2, pp. 223–235, Feb. 2005.
[21] H. K. Zhao, S. Osher, B. Merriman, and M. Kang, "Implicit and nonparametric shape reconstruction from unorganized data using a variational level set method," *Comput. Vis. Image Understanding*, vol. 80, pp. 295–314, 2000.
[22] S. Akkouche and E. Galin, "Implicit surface reconstruction from contours," *Vis. Comput.*, vol. 20, pp. 392–401, 2004.
[23] T. Surazhsky, V. Surazhsky, G. Barequet, and A. Tal, "Blending polygonal shapes with different topologies," *Comput. Graph.*, vol. 25, pp. 29–39, 2001.
[24] Y. Jeong and R. J. Radke, "Reslicing axially sampled 3-D shapes using elliptic Fourier descriptors," *Med. Image Anal.*, vol. 11, pp. 197–206, 2007.
[25] J. Serra, *Image Analysis and Mathematical Morphology*. New York: Academic, 1982.
[26] J. Serra, "Hausdorff distances and interpolations," in *Mathematical Morphology and its Applications to Image and Signal Processing*. Norwell, MA: Kluwer, 1998, pp. 107–114.
[27] V. Chatzis and I. Pitas, "Interpolation of 3-D binary images based on morphological skeletonization," *IEEE Trans. Med. Imag.*, vol. 19, no. 7, pp. 699–710, Jul. 2000.
[28] A. Bors, L. Kechagias, and I. Pitas, "Binary morphological shape-based interpolation applied to 3-D tooth reconstruction," *IEEE Trans. Med. Imag.*, vol. 21, no. 2, pp. 100–108, Feb. 2002.
[29] T. Y. Lee and W. H. Wang, "Morphology-based three dimensional interpolation," *IEEE Trans. Med. Imag.*, vol. 19, no. 7, pp. 711–721, Jul. 2000.
[30] G. Barequet, D. Shapiro, and A. Tal, "Multilevel sensitive reconstruction of polyhedral surfaces from parallel slices," *Vis. Comput.*, vol. 16, pp. 116–133, 2000.
[31] N. C. Gabrielides, A. I. Ginnis, and P. D. Kaklis, "Constructing smooth branching surfaces from cross-sections," in *Proc. 3rd ACM Symp. Solid Phys. Model.*, Beijing, 2007, pp. 161–170.
[32] D. Cohen-Or, A. Solomovici, and D. Levin, "3-D distance field morphing," *ACM Trans. Graph.*, vol. 17, no. 2, pp. 116–141, Apr. 1998.
[33] F. P. Kuhl and C. R. Giardina, "Elliptic fourier features of a closed contour," *Comput. Graph. Image Process.*, vol. 18, no. 3, pp. 236–258, 1982.
[34] B. Ballaro, F. Isgro, and D. Tegolo, "Silhouette encoding and synthesis using elliptic Fourier descriptors, and applications to videoconferencing," *J. Vis. Lang. Comput.*, vol. 15, pp. 391–348, 2004.
[35] H. Delingette, "On smoothness measures of active contours and surfaces," in *Proc. IEEE Workshop Variational Level Set Methods Comput. Vis.*, 2001, pp. 43–50.
[36] C. W. Chen, J. Luo, and K. J. Parker, "Image segmentation via adaptive k-mean clustering and knowledge-based morphological operations with biomedical applications," *IEEE Trans. Image Process.*, vol. 7, no. 12, pp. 1673–1683, Dec. 1998.

Alexandra Branzan Albu (M'07) received the B.S. degree in 1992, and the Ph.D. degree in 2000, both in electronic engineering, from the Polytechnic University of Bucharest, Romania.

In 2001, she joined the Computer Vision and Systems Laboratory at Laval University, QC, Canada, as a Postdoctoral Researcher and became an Assistant Professor in 2003. She is currently an Assistant Professor in the Department of Electrical and Computer Engineering, University of Victoria, BC, Canada. Her current research interests include medical imaging and computer vision-based human motion analysis.

Dr. Branzan Albu is a Professional Engineer affiliated to the Province of British Columbia Association of Professional Engineers. Since June 2007, she has been the Technical Program Chair of the IEEE Victoria Section.

Trevor Beugeling received the B.S. degree in mathematics from Simon Fraser University, BC, Canada, in 2002, and the B. Eng. degree in 2008 from the University of Victoria, where he is a Master's student with the Department of Electrical and Computer Engineering.

His current research interests include computer vision, cryptography, and signal coding.

Mr. Beugeling is the recipient of three Natural Sciences and Engineering Research Council of Canada (NSERC) undergraduate student research awards.

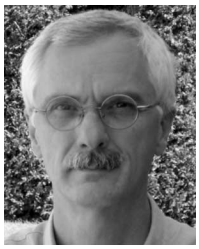

D. Laurendeau (M'81) received the B.S. degree in engineering physics in 1981, and the M.Sc. and Ph.D. degrees in 1983 and 1986, respectively, both in electrical engineering, all from Laval University, Quebec City, QC, Canada.

He is currently a Professor in the Department of Electrical and Computer Engineering, Laval University. In 1987, he was a Visiting Scientist at Hydro-Quebec Research Institute (IREQ). In 2001, he spent 6 months at ABB-Bomem as a Project Leader in the field of Fourier transform spectrometry for space applications. In 2005, he spent six months as a Visiting Scientist at Defense Research and Development Canada—Valcartier. His current research interests include computer vision, 3-D modeling for virtual reality, simulation in VR, object tracking, and biomedical applications of computer vision.

Dr. Laurendeau is a member of the Ordre des ingénieurs du Québec (OIQ), the Canadian Image Processing and Pattern Recognition Society (CIPPRS), and the International Association for Pattern Recognition (IAPR), for which he is currently the Secretary of the executive committee.